GAMMA-RAY BURSTS

Lecture Notes

Niccolò Bucciantini
INAF - Osservatorio Astrofisico di Arcetri

Spero che dopo aver letto questi appunti gli studenti non rimpiangano il giorno in cui decisero di fare Fisica, e non meledicano quello in cui io decisi di insegnarla.

CONTENTS

CHAPTER 1

GRBS: WHAT OBSERVATIONS TELL US

1.1 GRBs History and Phenomenology

GRBs are flashes of γ-rays, lasting about $1 - 100$ seconds. They were discovered in the late '60s by the VELA military satellites, shown in Fig. 1.1, launched by the US and aimed at spying russian nuclear activity. Fig. 1.1 shows the first γ-ray light curve ever measured, relative to the events GRB 670702 (July 2nd 1967).
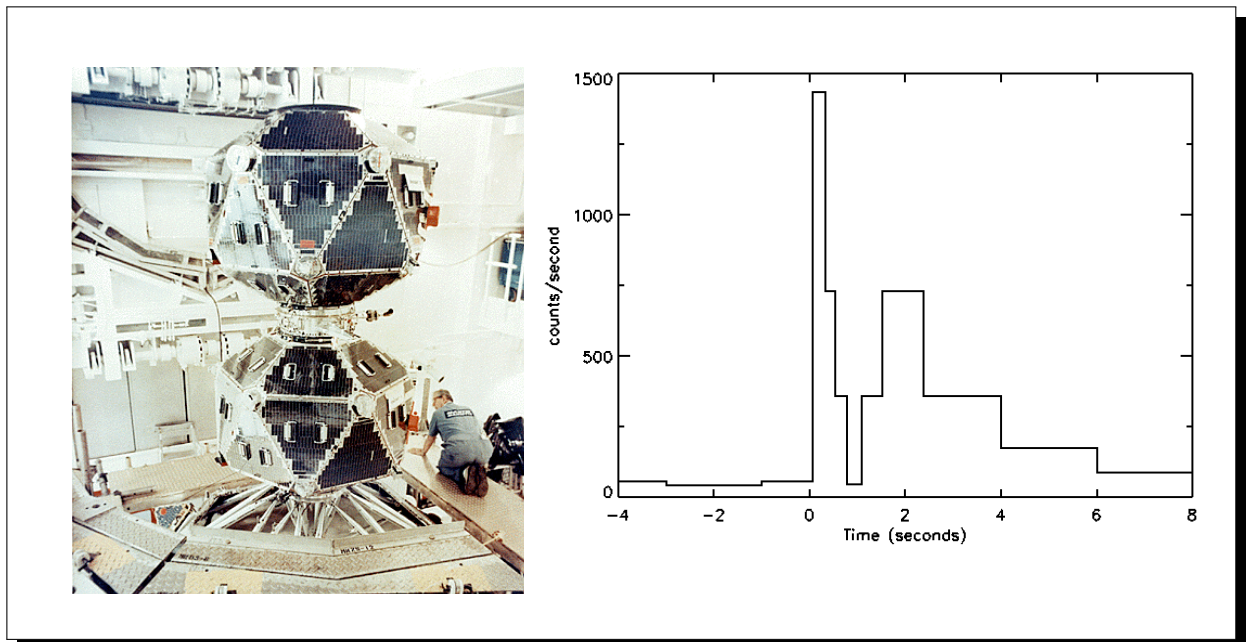

Figure 1.1: Left panel: one of the VELA satellites before launching. Right panel: γ-ray light curve of the first GRB event on July 2nd 1967.

Their detection was made public only in 1973, and by that time about 16 events had been recorded. Several models were put forward to explain these events, from nuclear flashes on NS and WD surfaces, to primordial BHs evaporation, but the paucity of data did not allow scientists to set meaningful constraints, in particular, without a determination of the distance, it was not possible to establish the energetics of these events. The science of GRBs had a major progress in 1991 thanks to the BATSE instrument on bord of the CGRO, Fig. 1.2, which operated until 2000. For the first time it was possible to measure with millisecond accuracy the light-curve of GRBs, to get a rough

estimate of their spectrum, and to locate their position. In the period from 1991 to 2000 BATSE measured about 8000 events, one every few days, and the first sky map, Fig. 1.2, immediately ruled out a galactic population. The events were compatible with an isotropic distribution, at all energies, showing no sign of either a disk component, or an overdensity in the direction of the Virgo Cluster. Of all the various models, only those invoking sources at cosmological distances, or in the solar neighborhood (at distance smaller than the disk scale-high ~ 100pc) were left to survive.
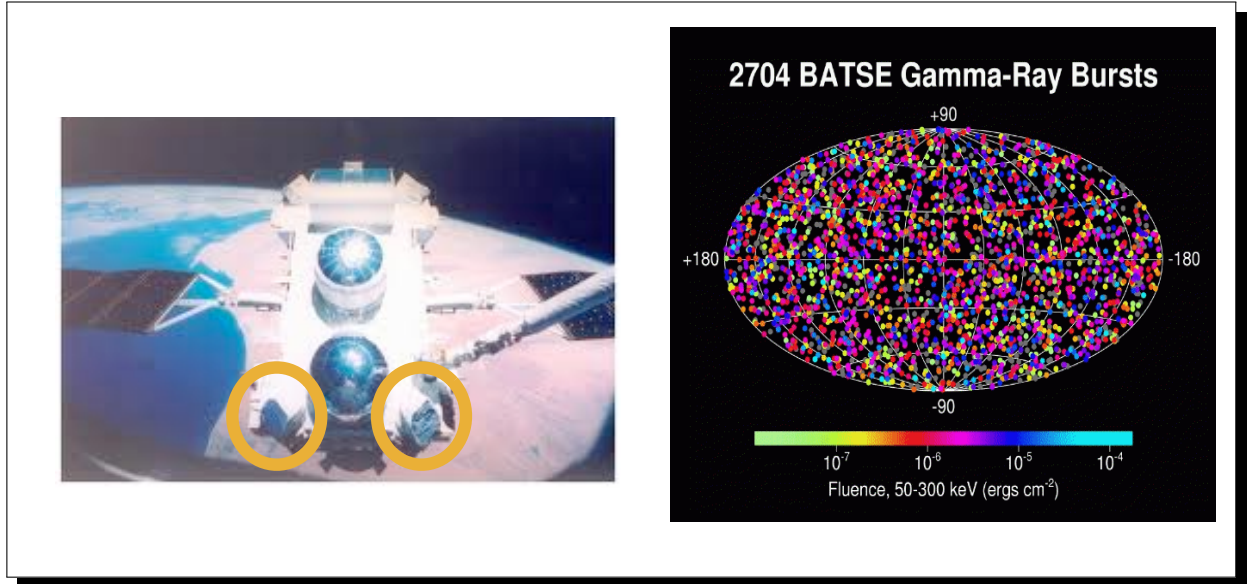

Figure 1.2: Left panel: the BATSE instruments (marked by the orange circles) on board of the CGRO. Right panel: the sky distribution of 2704 BATSE GRBs color-coded for their fluence.

Looking at BATSE light-curves, Fig. 1.3, it is immediately evident that the temporal evolution of the γ-ray luminosity can be extremely diverse: There are events with smooth evolution, others showing large variability up to millisecond timescales; some events are characterized by multiple peaks or flares; some have a very rapid rise time, others quite shallow.
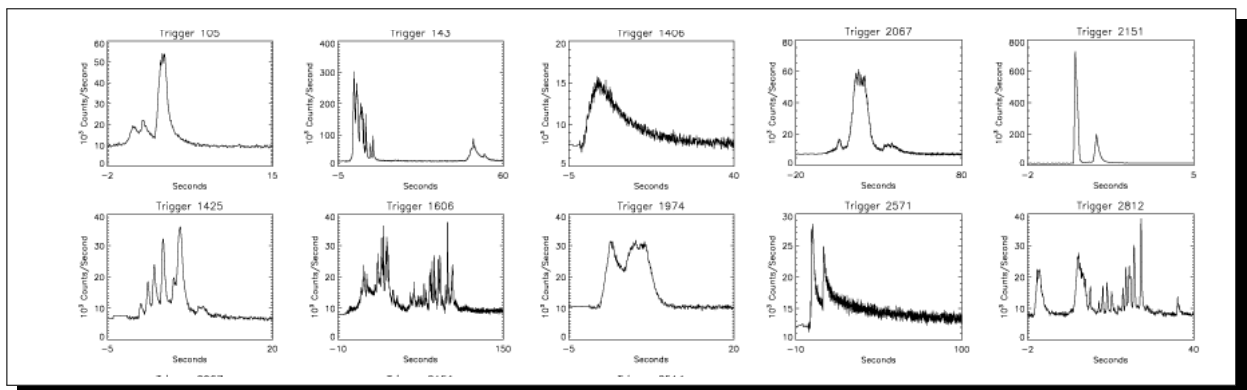
Figure 1.3: Light curves of various BATSE GRBs.

However thanks to the large number of events recorded by BATSE, it was possible to provide the first characterization of GRBs, based on two parameters: the so called *hardness ratio (HR)*, simply defined as the ratio of the energy detected in two different energy channels of the BATSE instrument, and the T_{90} time defined as time during which 90% of the GRB energy was detected. Fig. 1.4 shows the distribution of T_{90}. The distribution is bimodal and reveals the presence of two populations, one of long events (LongGRBs) with typical $T_{90} \gtrsim 2$s, and one of

short events (ShortGRBs) with typical $T_{90} \lesssim 2$s. Interestingly, these two populations, are distinct also in terms of the hardness ratio. The so called *hardness-duration* diagram in Fig. 1.4, shows that LongGRBs are softer and ShortGRBs are harder. About one fourth of all GRBs detected by BATSE is a Short one.
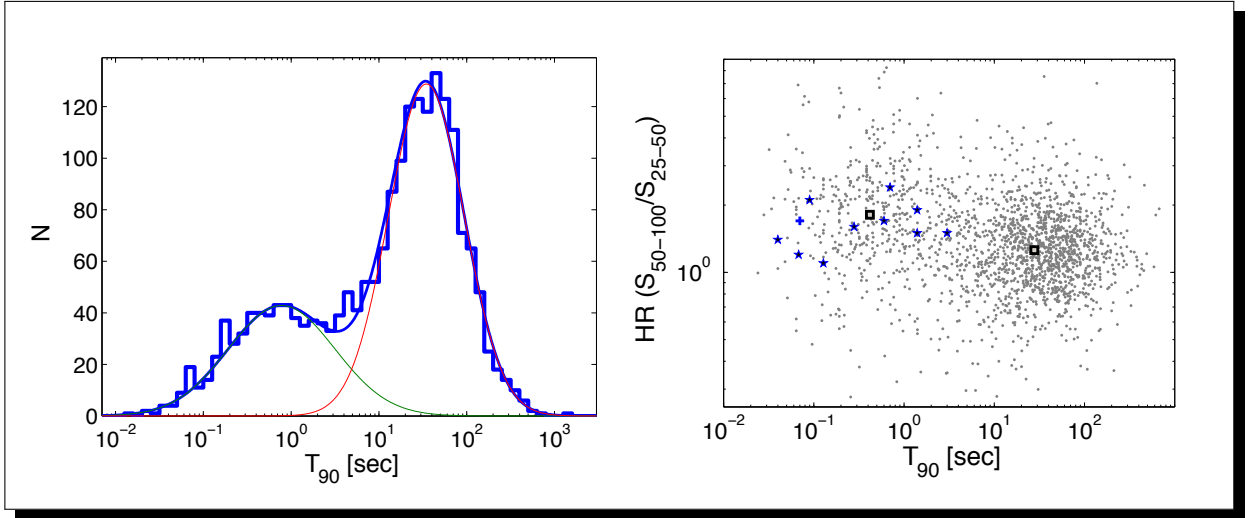

Figure 1.4: Left panel: the bimodal distribution of the T_{90} duration for 2041 GRBs in the BATSE GRBs catalogue. Superimposed are the decomposition of the distribution into two lognormal distributions (thin red and green solid lines) and their sum (thick solid blue line). Right panel: the duration T_{90} and the hardness ratio of 2000 GRBs from the BATSE catalog (grey dots), together with few Swift and HETE2 events (blue stars and crosses). Black squares mark the average logarithmic location of the ShortGRBs and LongGRBs population.

BATSE provided also the first determination of the time integrated γ-ray spectrum, of the prompt emission. Unlike their light curves, the time-integrated spectra of GRBs do not show the same extent of diversity. The majority of the BATSE GRB prompt emission spectra in the keV-MeV energy range were adequately fit with an empirical function called the Band function, Fig. 1.5, which consists of two power laws, smoothly connected together at the break energy E_{peak}, where the flux peaks. Typical values of power-law index for the low energy photon spectrum α, range from ~ -2 to ~ 0. Typical values of power-law index for the high energy photon spectrum β, range from ~ -4.5 to ~ -1.5 (note that values > -2 imply the presence of some high-energy cutoff, otherwise the total energy would diverge). E_{peak} has a quite narrow range from 100keV to 1MeV, with an average ~ 300keV, Fig. 1.6.
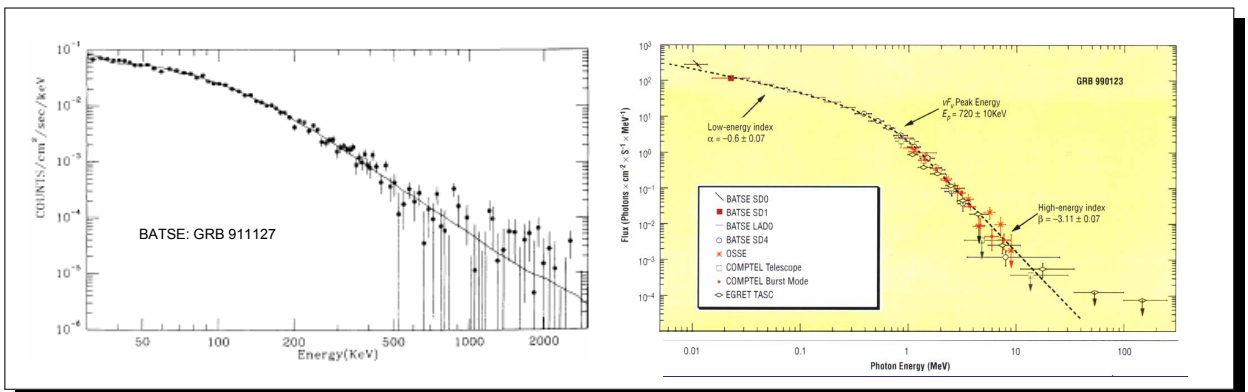

Figure 1.5: Left panel: count spectrum of GRB911127 with a Band function fit. Right panel: photon spectrum of GRB990123.
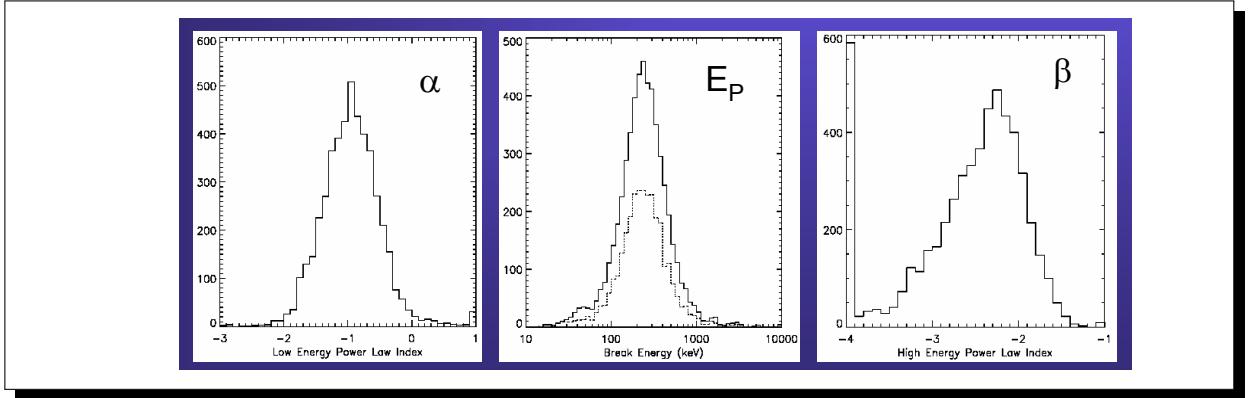
Figure 1.6: Distribution of power-law index for the low energy photon spectrum α (left), for the high energy photon spectrum β (right), and break energy E_{peak} (center), for GRBs in the BATSE catalogues, fitted with the Band function.

Unfortunately BATSE pointing accuracy $\sim 4°$ was not high enough to allow possible follow-up form ground based telescopes in order to identify possible optical counterparts. It was only with the launch of the Italian-Dutch satellite BeppoSAX, in 1996, that the identification of counterparts became possible. BeppoSAX was specifically design to allow rapid X-ray observation following a γ-ray trigger. Given the highest resolution of X-ray optics, it was possible to provide ground based facilities with high accuracy positions. On February 28th 1997 the first X-ray and optical afterglow of a GRB was detected. An optical galaxy was found in coincidence with the position of GRB 970228, Fig. 1.7, and the identification of absorption lines in its spectrum, allowed the first determination of a GRB red-shift. GRB 970228 was located at $Z = 0.695$. This firmly established GRBs as cosmological sources.
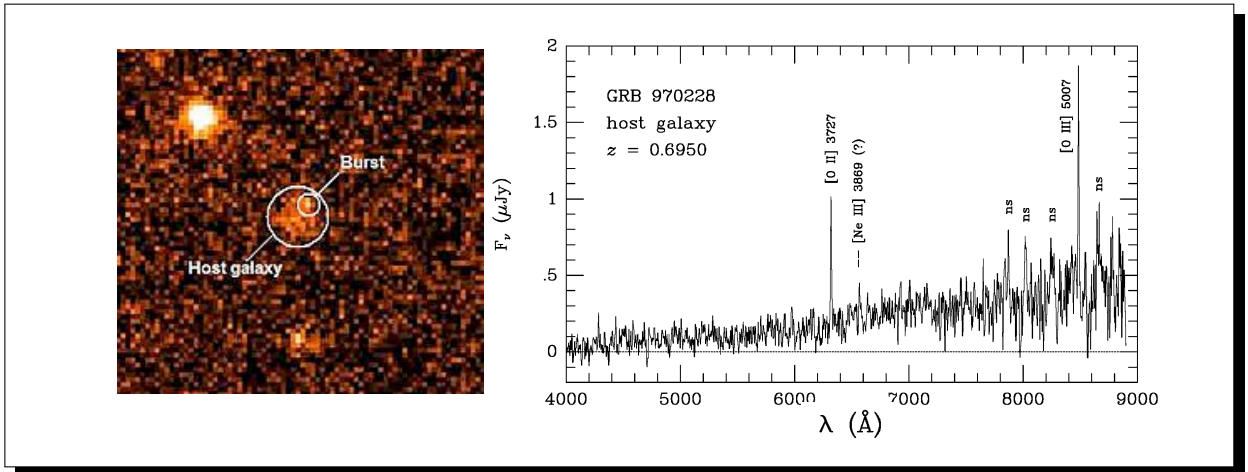
Figure 1.7: Left panel: HST image of the host galaxy of GRB 970228 together with the location of the optical afterglow. Right panel: optical spectrum of the host galaxy. Marked are the identified lines of [O II], [O III] and [Ne III] with their rest frame wavelength.

We now know that the majority of optically identified GRB host galaxies (almost all of them for LongGRBs) have redshift between $Z = 4$ and $Z = 1$, with a peak at $Z = 2$, as shown in Fig. 1.8. Noteworthy a few GRBs are detected at $Z > 8$ making them among the farthest objects known. These redshifts imply that the isotropic luminosity (the luminosity of an equivalent isotropic source) could be as high as 10^{52} erg s^{-1}, corresponding to a total isotropic energy emitted in γ-ray up to 10^{54} erg. In general it is found that LGRBs and SGRBs have similar luminosities, but LGRB are about two orders of magnitude more energetic. Moreover short GRBs are usually found at smaller redshifts, Fig. 1.8.

Figure 1.8: Left panel: distribution of the redshift of host galaxies of selected long GRBs. Right panel: redshift distribution for Long (light grey) and Short (dark grey) GRBs.

In 1998 for the first time, it was found an optical counterpart of a GRB in the SN 1998bw, Fig. 1.9. GRB 980425 is a Long one, and SN 19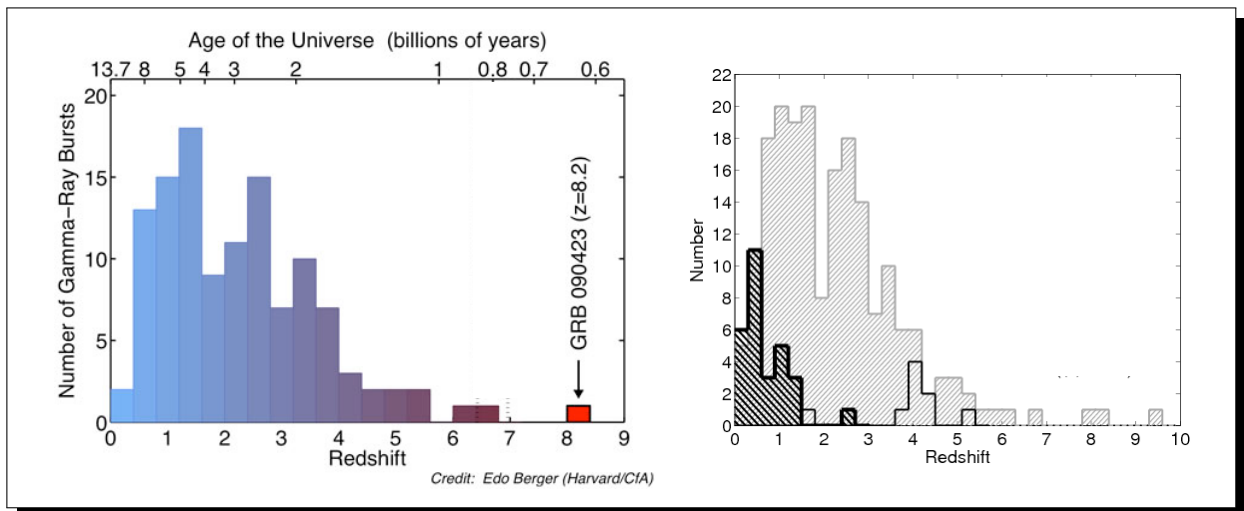98bw is a type Ic supernova. Type Ic SNe are core collapse SNe that show no H and He lines, and are usually associated to the death of massive stars $M > 30M_\odot$, that have lost their outer H and He envelope via powerful stellar winds (other possibilities include lower massive stars in a binary system that have lost their outer layers due to mass transfer in a common envelope phase, or convective star undergoing chemical mixing). Today we know about 20 GRB-SN firm associations (in several GRBs late time optical bump in the light-curve are often interpreted as the evidence of an underlying SN).
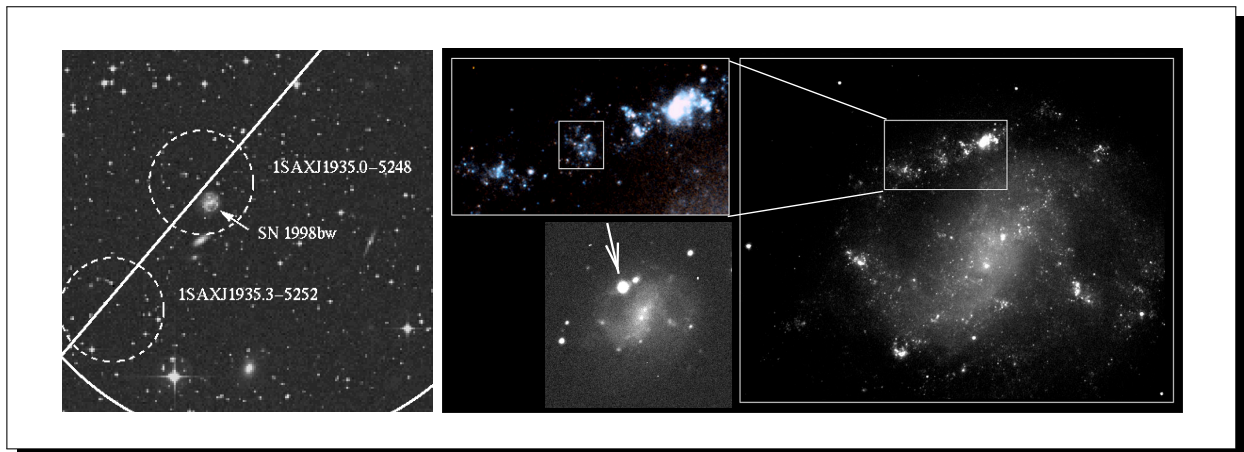
Figure 1.9: Left panel: DSS sky map if the region of GRB 980425. Dashed circles locate the position of two BeppoSAX sources detected in coincidence with the GRB. The arrow marks the host galaxy of SN 1998bw. Right panel: HST image of the host galaxy. The insert shows that the location where SN 1998bw exploded (see image below it) coincides with a star forming region.

The GRB-SN association was confirmed in 2003 by GBR 030329 associated with SN2003h, where it was possible to follow the evolution of the spectrum of the GRB into the spectrum of the SN: at early time the optical spectrum is dominated by the non-termal emission form the GRB afterglow, which fades out progressively letting the SN spectrum emerge at late time a shown Fig. 1.10. Today, apart from few rare events, where no SN was detected even in deep searches, we can say that all LGRB are possibly associated with SNe. In particular it is found that Long GRBs are associated to Type Ic supernovae, (on average there is one GRB every 100 SNe Ic), and that among

type Ic SNe, GRBs are associated with the ones having the highest velocity ejecta, and that are usually referred as Hypernovae.

Figure 1.10: Left panel: evolution of the optical spectrum of GRB 030329. During a period of 8 days it is possible to see that the spectrum of the optical afterglow changes from a simple power-law, to a more structured shape. Middle panel: optical residuals with respect to a pure power-law of the spectrum of GRB 030329 at 8 days, compared with optical spectra of the typical Type 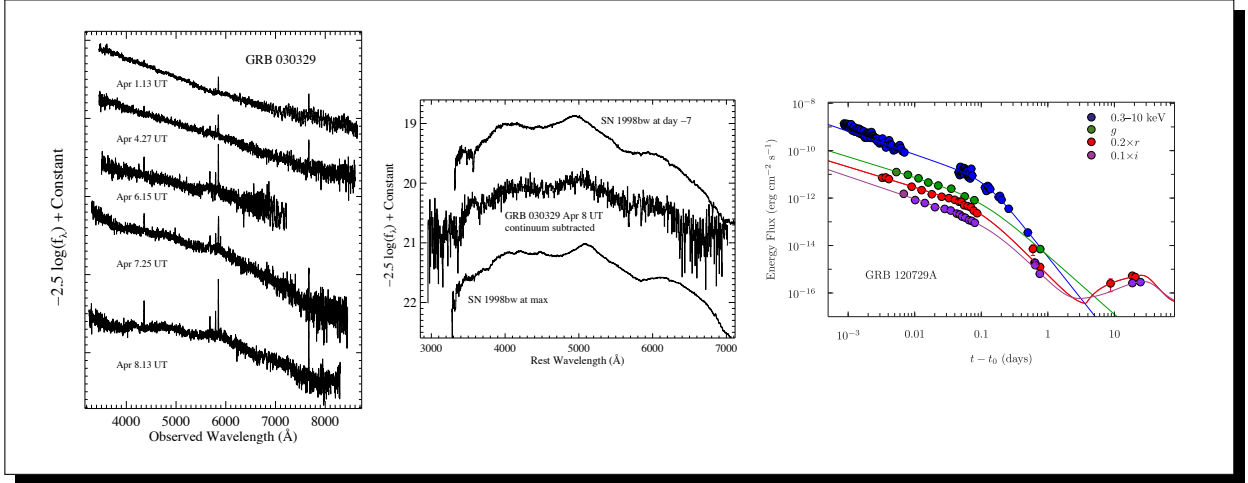Ic supernova SN 1998bw at similar times. Right panel: afterglow evolution of GRB 120729A in various bands. The optical-IR bump observed at ~ 10 days is interpreted as the emerging light from the associated SN.

Studies of X-ray and optical afterglows, enabled us to characterize the LGRBa and SGRB populations better than what could be simply done from the γ-ray prompt emission alone. Later, afterglows were discovered also in radio, hundreds of days after the prompt emission. It was found that SGRBs and LGRBs trace two distinct stellar populations. SGRBs are found in more massive galaxies including large spirals (Milkyway type) and elliptical, while LGRBs happen preferentially in smaller irregular blue galaxies with mass $\lesssim 10^{10} M_{\odot}$, Fig. 1.11. SGRBs select in general for older stellar populations, while LGRBs trace younger stars (they tend to be associated with star forming systems, and in general their redshift distribution tends to follow the high-mass star formation rate). They also differ in terms of their typical location within the host galaxy: SGRBs tend to be found at larger offset from the center than LGRBs. Moreover all SN-GRBs association are with Long one.
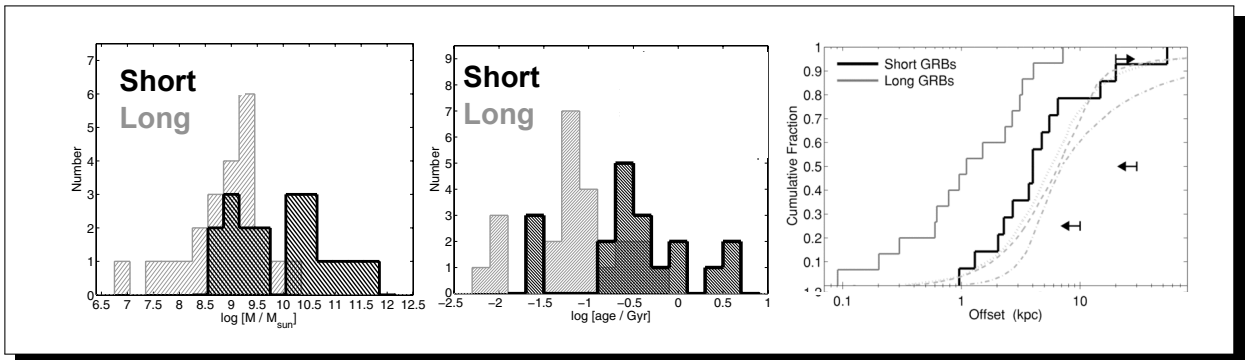

Figure 1.11: Left and Middle panels: stellar mass distribution and stellar age distribution of the host galaxies for Long and Short GRBs. Right panel: cumulative distribution of the offset of Long and Short GRBs with respect to the center of the galaxy.

This suggested that LBRGs should be associated with the death of massive stars, and might constitute the high energy tail of regular CC SNe. SGRBs are instead associated to an older population, and their canonical model invokes the coalescence of NS-NS or NS-BH binaries.

One of the most interesting phenomenology observed in the afterglow of GRBs was the presence of late time *jet-breaks*. Jet-breaks are achromatic changes in the light curve (a steepening), observed typically a few days after prompt emission, and that are interpreted as an evidence for the collimation of a decelerating outflow (see Sect. **??**). In Fig. 1.12, we show a typical example of jet-break, together with one of the fist study on the distribution of the jet-break time.
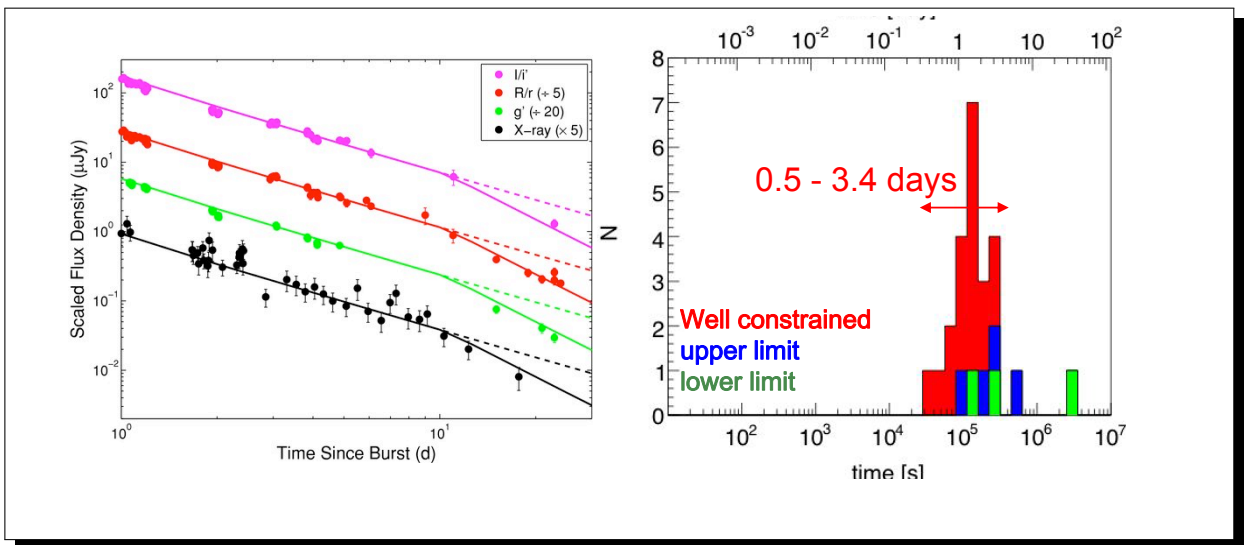
Figure 1.12: Left panel: example of achromatic jet-break; evolution of the afterglow light-curve in four different bands. Right panel distribution of observed jet breaks in Long-GRBs, as a function of time since burst.

In 2004 with the launch of the X-ray/UV satellite Swift, it became possible to conduct systematic studies of the afterglows of GRBs. The most interesting phenomenology discovered with Swift was the so called *late time activity* present in the afterglow, Fig. 1.13. By late time activity, we mean evidence in the afterglow, of some kinds of late time energy injection, either in the form of plateaus, or in the form of flares/rebrightenings. These are also observed in Short GRBs, about 100-1000 second after the prompt emission. Such energy injection demanded a long lasting engine, setting strong constraints on the possible mechanism at the origin of GRBs.
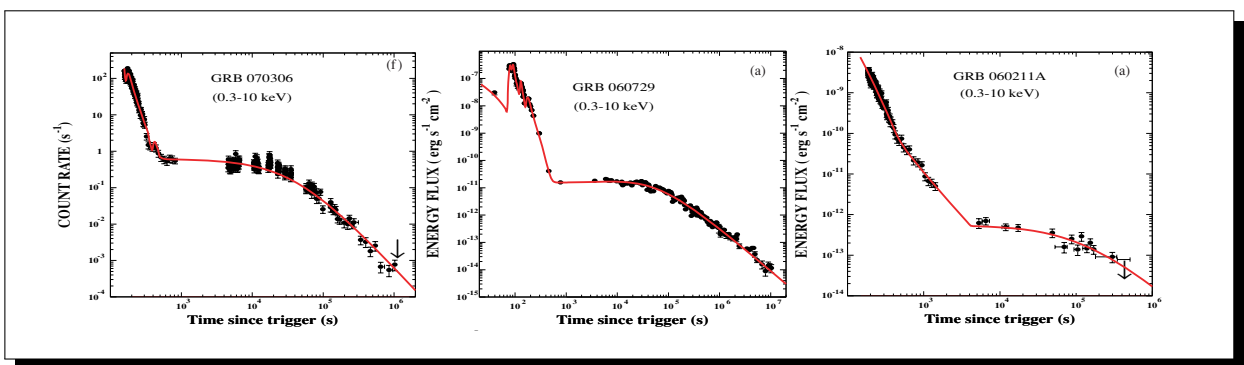
Figure 1.13: Examples of late time activity in the form of plateaus in the light curve of the X-ray afterglow of Long GRBs.

1.1.1   Canonical Models for GRBs Engines

The key observations that constrain the possible engines for Long and Short GRBs, are the short time scale variability and the large isotropic energy. The observed millisecond variability implies central engines with typical sizes of ~ 10 km. The large isotropic energy, comparable with the rest mass of a $1 M_\odot$ object, corresponding to typical beaming corrected energies $\sim 10^{52}$ erg, implies a mechanism with very large efficiency. Moreover the possible engine must be compatible with the typical stellar population characteristic of the GRB environment.

There are two canonical models for the engine of Long GRBs. The *collapsar model* is based on the idea that the core of massive stars (recall that Long GRBs are associated to the death of massive stars, $M > 30 M_\odot$), collapses directly to Black Hole. Matter of the outer layers then falls onto the BH: while along the polar axis matter can be directly accreted, leaving and evacuated funnel, along the equator, centrifugal support leads to the formation of an accretion disk. It is the accretion of the outer layer that powers the GRBs, leading to a jet that propagates along the evacuated polar funnel. In the collapsar model, the mass accretion rate, which is dictated by the structure of the surrounding star, regulates the energy injection. The origin of the relativistic outflow is less clear: it could originate from a disk wind, from neutrino-antineutrino annihilation in the disk corona, or from the Bladford-Znajeck mechanism tied to the rotation of the BH itself. The main problems of the collapsar model are that: it does not explain why the supernova looks like any other type Ic SN, or what drives the SN (the original collapsar model predicted SN-less GRBs), it does not put tight constraints on the energetics, it requires large angular momentum in the BH, it is not clear what powers late activity.

More recently an alternative model, the *millisecond magnetar model*, has been put forward, to address some of those issues. The idea behind the millisecond-magnetar model is that the core of a massive star does not collapse directly to BH, but forms a rapidly rotating NS with magnetar like magnetic field. A simple estimate using the dipole spin-down formula, suggests that a millisecond rotator with a magnetic field $\sim 10^{15}$G, could lose $\sim 10^{52}$ erg of energy in ~ 100s, enough to power a Long GRB. The formation of a NS is more in line with standard models for SNe, and fits naturally in the GRB-SN connection. The angular momentum requirements are less severe than for BHs, and the spin-down evolution sets strong constraints on the energetics, that can be tested. The main problem with this model is that it fails to predict very Long GRBs ($t_{90} > 300$s), or GRBs with major rebrigthnings. On the other hand it naturally provides a long lasting engine that can power the late activity.

For Short GRBs the canonical model invokes the merger of a binary NS. It was originally proposed that such mergers could lead to the formation of a rapidly rotating BH. During the merger about $10^{-3} M_\odot$ are left over to form a disk that can accrete, on typical timescales ~ 1s, powering a Short GRBs. However the presence of late activity and energy injection (in Short GRBs the energy necessary for late activity is comparable to the one powering the prompt phase), typically after 100s, is vey hard to justify. For this reason it was poposed that instead of directly collapsing to BH the merger could lead to a rapidly rotating long-live (supra-massive) NS. If this NS has magnetar like magnetic fields than the millisecond magnetar model could apply. The presence of a millisecond-magnetar could naturally explain the late-activity.

1.2   GRBs are relativistic

There are several arguments based on simple observations of the temporal evolution and spectral properties of the prompt γ-ray emission of GRBs, and their late Radio behavior, that immediately allow one to conclude that GRBs must be associated to relativistically expanding systems.

1.2.1 Cavallo Rees Relation

There is a very important limit that can be placed on the ratio of the luminosity and typical timescale of an astrophysical source. For an astrophysical source of size R with luminosity L lasting for a time Δt the total energy must be $L\Delta t$, and it will be related to the mass contained in the source by:

$$L\Delta t = \eta \frac{4\pi}{3} R^3 n m_p c^2 \tag{1.1}$$

where n is the baryonic density, m_p the proton mass, and $\eta < 1$ is the efficiency of matter to energy conversion. For an instantaneous injection (the duration of the spike ~ 1s is much longer than the typical timescales at the base of the NS magnetosphere $\sim R/c \sim 10^{-3}$ s) the duration of the source is related to the time it takes for a photon to escape.

$$\Delta t > \frac{R}{c}(1 + \tau_{\mathrm{T}}) \tag{1.2}$$

where R/c is the light crossing time and τ_{T} the optical depth. The correction comes from the fact that for $\tau_{\mathrm{T}} > 1$ photons diffuse with a random walk and the escape time increases accordingly. The opacity for a fully ionized system ($E_{\mathrm{peak}} \sim 300$ keV) is just the Thompson opacity due to electrons $\tau_{\mathrm{T}} = \sigma_{\mathrm{T}} n R$, where we have assumed one electron per baryon (the case of H). Combining Eq. 1.1 and 1.2 to simplify the radius, one has:

$$\Delta t > \frac{3}{4\pi} \frac{\sigma_{\mathrm{T}}}{m_p c^4} \frac{L}{\eta} \frac{(1 + \tau_{\mathrm{T}})^2}{\tau_{\mathrm{T}}} \quad \Rightarrow \quad L < \frac{4\pi}{3} \frac{m_p c^4}{\sigma_{\mathrm{T}}} \frac{\tau_{\mathrm{T}}}{(1 + \tau_{\mathrm{T}})^2} \eta \Delta t < \frac{\pi}{3} \frac{m_p c^4}{\sigma_{\mathrm{T}}} \eta \Delta t \tag{1.3}$$

given that the maximum is for $\tau_{\mathrm{T}} = 1$. One then has:

$$\frac{L}{\Delta t} < 2\eta \times 10^{42} \mathrm{erg\ s^{-2}} \tag{1.4}$$

This in known as *Cavallo-Rees* limit, and it does not depend on any property of the source. In Long GRBs The typical isotropic energy E_{iso} is of the order of 10^{53} erg, while the typical duration is $\Delta t \sim 100$s, leading to $\frac{L}{\Delta t} \approx 10^{49}$ erg s^{-2}, about 7 orders of magnitude higher than the above limit.

The Cavallo-Rees limit assumes a source that does not expand at relativistic speeds, such that the light crossing time is strictly related to the observed duration. For a system expanding at the speed of light this is not so. Let us assume that the first photon is emitted when the typical size of the system is R_i, and the last photon is emitted after a time Δt_{true} when the size of the system is R_f. Now if the system expands at a high Lorentz factor γ, then the velocity is $v \simeq 1 - 1/2\gamma^2$, and $R_f = R_i + v\Delta t_{\mathrm{true}}$. As a consequent the difference in the arrival time of the two photons will be:

$$\Delta t_{\mathrm{obs}} = \Delta t_{\mathrm{true}} - \frac{R_f - R_i}{c} = \frac{\Delta t_{\mathrm{true}}}{2\gamma^2} \tag{1.5}$$

on the other hand the due to doppler boosting the observed luminosity will be a factor γ times higher than the intrinsic one (the energy of each photon is γ times higher). So the correct relation in terms of observed quantities will be:

$$\frac{L_{\mathrm{obs}}}{\Delta t_{\mathrm{obs}}} < \gamma^3 \frac{L_{\mathrm{true}}}{\Delta t_{\mathrm{true}}} < 2\eta\gamma^3 \times 10^{42} \mathrm{erg\ s^{-2}} \tag{1.6}$$

that can be satisfied as long as $\gamma \gtrsim 100$.

1.2.2   Compactness

GRBs show a spectrum where the majority of photons have typical energies $\sim E_{\text{peak}} \sim 300\text{keV}$. This implies that, taken any two photons, a large fraction of them will satisfy the relation $\sqrt{h^2\nu_1\nu_2} > m_e c^2$, such that in principle they can interact leading to pair-production. In particular it is often observed an high-energy power-law tails of photons extending all the way to GeV energies, as shown in Fig. 1.14. These photons can in principle pair produce over the bulk of the other photons (all the way down to $\sim 1\text{keV}$). Let us compute the pair-creation optical depth for those photons. For a non relativistic system the photon number density if just the total radiated energy divided by the source volume and typical photon energy. For photons at 1GeV interacting with the bulk photons with typical energy $\sim E_{\text{peak}}$ the value of $\sqrt{h^2\nu_1\nu_2} \simeq 10 m_e c^2$, which implies a typical cross section for pair creation $\sim 10^{-1}$ times the Thompson cross section σ_{T}, as shown in Fig. 2.1. Then one finds:

$$\tau_{\gamma\gamma} \approx 0.1\sigma_{\text{T}} \left(\frac{E_{\text{iso}}}{E_{\text{peak}}}\right) R^{-2} \approx 10^{12} \left(\frac{\Delta t}{1\text{s}}\right)^{-2} \tag{1.7}$$

where we have taken $E_{\text{iso}} \sim 10^{53}\text{erg}$, and $R = c\Delta t$. This is so much larger than unity that there should be no photon at those energies, while we do see them, and we see also a non-thermal distribution.
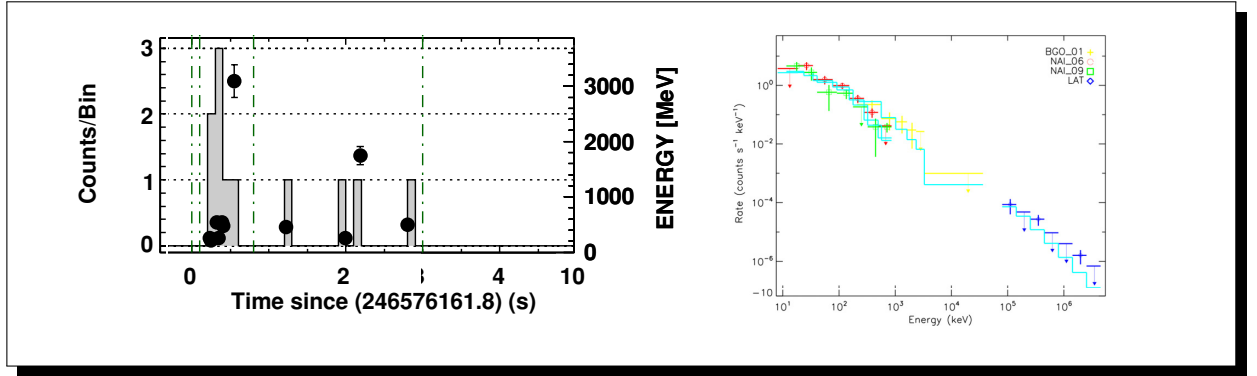

Figure 1.14: Left panel: events count for high energy photons above 0.1GeV, detected by Fermi-LAT, in the first few seconds of GRB 081024B. Right panel: reconstructed spectrum of GRB 081024B up to a few GeV (see the last LAT point).

However for a source expanding with a high Lorentz factor the relation between the observed duration and the true source size is $R_{\text{true}} = 2\gamma^2 c\Delta t_{\text{obs}}$. Moreover photons having an observed energy E_{obs} will have an energy in the reference frame of the system where they pair produce $\sim E_{\text{obs}}/\gamma$. The same will hold for the bulk of photons whose energy will be E_{peak}/γ. So a GeV photon (produced as a $E_1 = \gamma^{-1}\text{GeV}$ in the reference frame of the expanding system) will only be able to interact with other high energy photons ($E_2 \geq m_e^2 c^4/E_1 \approx \gamma\text{keV} \gg E_{\text{peak}}/\gamma$) in the reference frame of the expanding system. A GeV photon will interact with other $\gamma^2\text{keV}$ photons. So only the $\gamma^2\text{keV}$ photon density will matter:

$$N_{h\nu>\gamma^2\text{keV}} \approx N_{\text{tot}} \left(\frac{\gamma^2\text{keV}}{E_{\text{peak}}}\right)^{1-\beta} = N_{\text{tot}} \left(\frac{\gamma^2}{100}\right)^{1-\beta} \tag{1.8}$$

where $\beta \sim 2.2$ is the high energy photon index. Hence the correct estimate for the GeV opacity wil be:

$$\tau_{\gamma\gamma} \approx 0.1\sigma_{\text{T}} \left(\frac{E_{\text{iso}}}{E_{\text{peak}}\gamma^{2\beta-2}}\right) R_{\text{true}}^{-2} \approx \frac{10^{12}}{\gamma^{2+2\beta}} \left(\frac{\Delta t_{\text{obs}}}{1\text{s}}\right)^{-2} \quad \Rightarrow \quad \gamma \gtrsim 10^2 \tag{1.9}$$

in order for the system to be optically thin up to GeV.

1.2.3   Radio Scintillation

It is well known that light propagation through a turbulent medium, with varying refractive index, gives rise to *scintillation*: rapid variations in the intensity of a point source. Scintillation is observed in Radio for both galactic (pulsars) and extragalactic (AGNs) sources, and is related to the fluctuations in the electron density of the ISM. For a light ray, of wave number $k = 2\pi/\lambda$ propagating in a medium with a density of free electron n_e the refractive index is given by:

$$\eta = 1 - 4\pi \frac{n_e r_o}{k^2} \tag{1.10}$$

where $r_o = e^2/(m_e c^2)$ is the classical electron radius. Light propagating through a clump of side δx with a fluctuation in electron density δn_e, will accumulate a phase lag with respect to a neighboring average region, corresponding to a difference in optical path:

$$\delta l = \delta x \delta \eta = 4\pi k^{-2} r_o \delta n_e \delta x \tag{1.11}$$

As the light propagates through a turbulent layer of size D it will encounter $\sim D/\delta x$ clumps. The contribution to the various clumps will add incoherently such that the effect of the turbulent layer will be to produce a typical total difference in optical path:

$$\delta l_{\rm tot} = \delta x \delta \eta \left(\frac{D}{\delta x} \right)^{1/2} = 4\pi k^{-2} r_o \delta n_e (D \delta x)^{1/2} \tag{1.12}$$

Now if the electron density is distributed according to a power-law, like for example in the case of Kolmogorov turbulence, then:

$$\delta n_e^2(\tilde{k}) \propto C_n^2 \tilde{k}^{-q} \quad \Rightarrow \quad \delta n_e^2(\delta x) = \int_{1/\delta x}^{\infty} C_n^2 \tilde{k}^{-q} d\tilde{k} = C_n^2 \delta x^{q-1} \tag{1.13}$$

where the integral is done on all the contributions of the fluctuations at scales smaller than δx (larger scales do not contribute to phase differences). For Kolmogorov turbulence $q = 5/3$. Then one finds:

$$\delta l_{\rm tot} = 4\pi k^{-2} r_o \delta n_e (D \delta x)^{1/2} = 4\pi k^{-2} r_o D^{1/2} \delta x^{q/2} C_n \tag{1.14}$$

Immagine now that the turbulence is confined into a *thin screen* at distance z_{sc} from the observer. On such a screen the size of a coherent region (a region where the wave front phase difference is smaller than the wavelength itself, such that interference can take place) will be given by the condition:

$$\delta l_{\rm c} \lesssim k^{-1} \quad \Rightarrow \quad \delta x \lesssim (16\pi^2 r_o^2 C_n^2 D k^{-2})^{-3/5} = (4 r_o^2 C_n^2 D \lambda^2)^{-3/5} \tag{1.15}$$

Such coherent size, corresponds to the angular size of a point like source (the minimal resolvable size, given that the turbulent screen behaves a an interferometer that introduces phase shift among neighboring elements). Above this distance different part of the screen will only interfere incoherently. Below this distance interference will be coherent, and a diffraction pattern will be generated (as in the case of an interferometer). As the observer moves across this diffraction pattern, strong scintillation will arise. Obviously, scintillation can only take place if the source angular size is smaller than the angular size corresponding to a coherent patch:

$$\theta_{\rm s} = \frac{\delta l_{\rm c}}{z_{sc}} \lesssim (4 C_n^2 D r_o^2 \lambda^2)^{-3/5} z_{sc}^{-1} \approx 2.25 \left(\frac{\lambda}{3 {\rm cm}} \right)^{6/5} \left(\frac{z_{sc}}{1 {\rm kpc}} \right)^{-1} \mu \ {\rm arcsec} \tag{1.16}$$

where we have taken Radio wavelength, we have chosen a typical distance of the turbulent layer of the order of the size of the galactic disk, and we have taken $C_n^2 D \sim 10^{-3.5} {\rm m}^{-20/3} {\rm kpc}$ as derived from pulsar scintillation.

For a cosmological source located at a few Gpc from us, such angular size corresponds to a real size $\sim 10^{17}$ cm. Larger sources will not experience strong scintillation.

As shown in Fig. 1.15, strong scintillation in radio is observer in the first 30-50 days after the burst, with radio luminosity setting to a less variable trend at later times. This means that in a timescale of the order of 30 days $\sim 3 \times 10^6$ seconds, the source expand to a size $> 10^{17}$ cm, implying expansion velocity close to the speed of light.
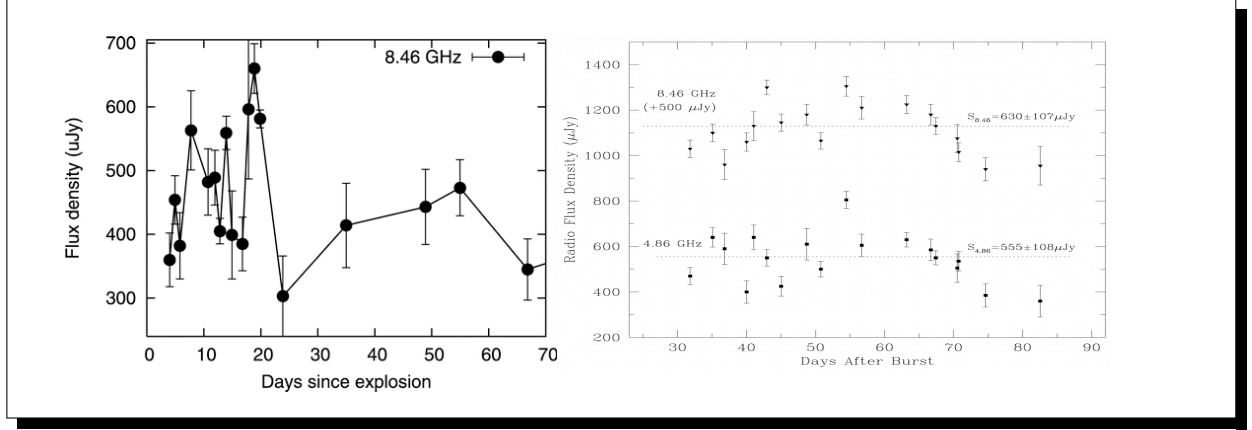
Figure 1.15: Left panel: radio flux density of GRB 070125. Right panel: radio flux density of GRB 970508.

1.3 GRBs are collimated

Given that GRBs are highly relativistic outflows, only a small portion of their emitting surface will be observable. Assuming a radial expansion with a Lorentz factor γ, each element of the emitting surface will produce radiation that is beamed into a cone of opening angle $1/\gamma$. If the observer direction lays outside this cone, then photons will not be detected. As a result only a small portion of the emitting surface, an area of opening angle $1/\gamma$ around the direction of the observer, will be visible. As the outflow expands into the surrounding medium, matter will be collected in front of it, such that it will slow down. Before the outflow becomes non-relativistic (which, as we saw, happens at about 30 days after the prompt emission), the evolution of the front can be described by the Blandford-McKee solution:

$$\gamma = \left(\frac{17E}{8\pi\rho_o} \right)^{1/2} t^{-3/2} \tag{1.17}$$

Recalling that for a moving source the true time is related to the observed time by $t = 2\gamma^2 t_{\rm obs}$, we find the relation:

$$\gamma = \left(\frac{17E}{8\pi\rho_o} \right)^{1/8} t_{\rm obs}^{-3/8} \tag{1.18}$$

As a consequence as the flow slows-down a progressively larger fraction of the emitting surface will be visible. Let us assume that the intrinsic surface luminosity goes like $t^{-\alpha}$ then the observed luminosity once integrated over the observable surface will go like: $t^{-\alpha} R(t)/\gamma^2 = t^{4-\alpha} \propto t_{\rm obs}^{2-\alpha/2}$.

However in the late afterglow, at a few days after prompt emission, it is often observed an achromatic change in the temporal evolution of the observed luminosity (a change in the time-slope). Being achromatic, it cannot be due to either cooling, or a change in the acceleration properties (for example efficiency), or the opacity of the emitting surface, because such processes are usually dependent on the energy of the emitting particles, and they tend to show as chromatic effects.

Such achromatic changes are usually referred as *jet-breaks* because they are commonly interpreted as geometric effects related to the finite extent of the emitting surface. If the total emitting surface has a typical angular extent $\theta_{\rm jet}$, as it is the case for a jet, then there will be two different regimes if either $1/\gamma < \theta_{\rm jet}$ when only a portion of the surface will be visible (a portion that increases as the flow slows-down), or $1/\gamma > \theta_{\rm jet}$ when the entire surface will

be visible (and further slowing-down will have no effect). In this latter case the observed luminosity will go like $t^{-\alpha}R(t)^2\theta_{\text{jet}} = t^{1-\alpha} \propto t_{\text{obs}}^{(1-\alpha)/2}$, decreasing much faster. A typical example of jet break is shown in Fig. 1.12 (note that the slope change is just 1 and not 1.5, probably because the expansion is not in a uniform medium), together with the typical jet-break time. Now once the ratio E/n of the energy of the explosion over the ambient density is known (can be derived from the later Sedov calorimetry, see Sect. 1.4), from the observed jet-break time it is possible to infer the jet opening angle:

$$t_{\text{jb}} \approx 4(1+z) \left(\frac{E_{53}}{n_o}\right)^{1/3} \left(\frac{\theta_{\text{jet}}}{0.2}\right)^{8/3} \text{days} \tag{1.19}$$

where E_{53} is the isotropic energy in units of 10^{53}erg, n_o is the ambient density in units cm^{-3}, and z is the redshift. In Fig. 1.16 we show the statistics of jet opening angles.
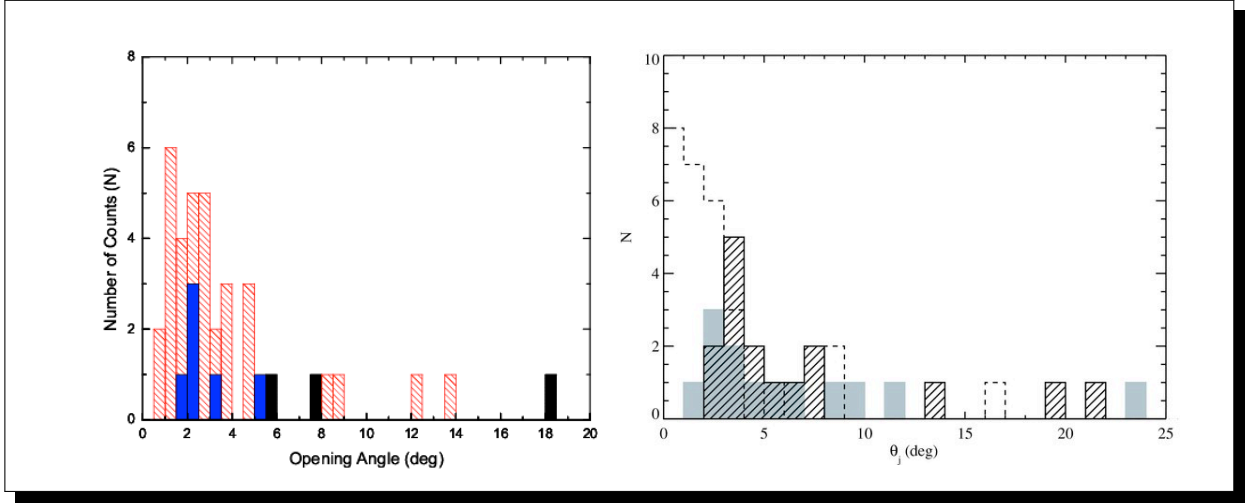

Figure 1.16: Typical jet opening angle derived from jet-breaks. The various color-styles refer to GRB samples with different selection criteria. The distribution peaks at a few degrees.

1.4 Radio Calorimetry of GRBs in the late Sedov Phase

Once the expansion speed of the forward shock becomes non relativistic $\gamma \sim 1$, beaming effects and Doppler boosting become negligible, and one can use simple non-relativistic derivations. The only effect that still needs to be taken into account is the cosmological redshift. This implies that the radiation from the entire blast wave is visible. We are thus in a good position to estimate its total energetics. We are going here to show how the late radio spectral evolution can be used to constrain the total energetics of the explosion.

1.4.1 Synchrotron Emissivity and Absorption Coefficient for a Power-law Distribution

Let us assume that the emitting particles can be described as a power-law in energy beginning at a minimum Lorentz factor γ_m to $\gamma \to \infty$: $N(\gamma) = N_m(\gamma/\gamma_m)^{-p}$. The normalization constant is related to the particle density as:

$$n = \int_{\gamma_m}^{\infty} N_m \left(\frac{\gamma}{\gamma_m}\right)^{-p} d\gamma = N_m\gamma_m \int_1^{\infty} \left(\frac{\gamma}{\gamma_m}\right)^{-p} d\frac{\gamma}{\gamma_m} = \frac{N_m\gamma_m}{p-1} \quad \Rightarrow \quad N_m = \frac{(p-1)n}{\gamma_m} \tag{1.20}$$

For synchrotron emission one can define the following quantity: the characteristic frequency ν_c of a particle with Lorentz factor γ; the characteristic frequency ν_m of particles with $\gamma = \gamma_m$; the synchrotron power per unit frequency $P(\nu, \gamma)$ emitted by a single electron with Lorentz factor γ and mediated over pitch angle:

$$\nu_c = \gamma^2 \left(\frac{eB}{2\pi m_e c} \right), \qquad \nu_m = \gamma_m^2 \left(\frac{eB}{2\pi m_e c} \right) \tag{1.21}$$

$$P(\nu, \gamma) = \frac{e^3 B}{m_e c^2} F \left[\frac{\nu}{\nu_c} \right] = \frac{e^3 B}{m_e c^2} F \left[\frac{\nu}{\nu_m} \frac{\gamma_m^2}{\gamma^2} \right] \tag{1.22}$$

It is found that the average over pitch angle changes marginally the value of F with respect to the orthogonal case $F(x) \sim 1.5x \int_x^\infty K_{5/3}(\zeta) d\zeta$.

We introduce the following auxiliary function:

$$F_k[x] = \int_0^x F[y] y^{(p-k)/2} dy \tag{1.23}$$

It is now possible to compute the synchrotron emissivity for unit volume, recalling that $2d\gamma = -\gamma^3 d(1/\gamma^2)$:

$$
\begin{aligned}
j_\nu &= \int_{\gamma_m}^\infty P(\nu, \gamma) N(\gamma) d\gamma = \frac{e^3 B}{m_e c^2} \int N_m \gamma_m \left(\frac{\gamma}{\gamma_m} \right)^{-p} F \left[\frac{\nu}{\nu_m} \frac{\gamma_m^2}{\gamma^2} \right] d\frac{\gamma}{\gamma_m} \\
&= \frac{e^3 B}{m_e^2 c^2} \gamma_m N_m \int \left(\frac{\gamma_m^2}{\gamma^2} \right)^{\frac{p}{2}} F \left[\frac{\nu}{\nu_m} \frac{\gamma_m^2}{\gamma^2} \right] \frac{-\gamma^3}{2\gamma_m^3} d\frac{\gamma_m^2}{\gamma^2} \\
&= -\frac{e^3 B}{2m_e^2 c^2} \gamma_m N_m \int \left(\frac{\gamma_m^2}{\gamma^2} \right)^{\frac{(p-3)}{2}} F \left[\frac{\nu}{\nu_m} \frac{\gamma_m^2}{\gamma^2} \right] d\frac{\gamma_m^2}{\gamma^2} \\
&= -\frac{e^3 B}{2m_e^2 c^2} \gamma_m N_m \left(\frac{\nu}{\nu_m} \right)^{\frac{(1-p)}{2}} \int \left(\frac{\nu}{\nu_m} \frac{\gamma_m^2}{\gamma^2} \right)^{\frac{(p-3)}{2}} F \left[\frac{\nu}{\nu_m} \frac{\gamma_m^2}{\gamma^2} \right] d\left(\frac{\nu}{\nu_m} \frac{\gamma_m^2}{\gamma^2} \right) \\
&= \frac{e^3 B}{2m_e^2 c^2} \gamma_m N_m \left(\frac{\nu}{\nu_m} \right)^{\frac{(1-p)}{2}} F_3 \left[\frac{\nu}{\nu_m} \right] = (p-1) \frac{e^3 B}{m_e^2 c^2} n \nu_m^{\frac{(p-1)}{2}} \nu^{\frac{(1-p)}{2}} F_3 \left[\frac{\nu}{\nu_m} \right] \\
&= \frac{(p-1)}{2} n \gamma_m^{p-1} \left(\frac{e^3 B}{m_e^2 c^2} \right) \left(\frac{eB}{2\pi m_e c} \right)^{(p-1)/2} \nu^{(1-p)/2} F_3 \left[\frac{\nu}{\nu_m} \right]
\end{aligned}
\tag{1.24}
$$

where we have used the fact that for any function G:

$$-\int_{\gamma_m}^\infty G \left[\frac{\nu}{\nu_m} \frac{\gamma_m^2}{\gamma^2} \right] d\left(\frac{\nu}{\nu_m} \frac{\gamma_m^2}{\gamma^2} \right) = \int_o^{\nu/\nu_m} G[y] dy \tag{1.25}$$

Similarly we can compute the absorption coefficient:

$$
\begin{aligned}
\alpha_\nu &= \frac{(p+2)c^2}{8\pi\nu^2}\int_{\gamma_m}^\infty \frac{P(\nu,\gamma)}{m_ec^2}\frac{N(\gamma)}{\gamma}d\gamma = \frac{(p+2)c^2}{8\pi\nu}\frac{e^3B}{m_ec^2}\int N_m\left(\frac{\gamma}{\gamma_m}\right)^{-(p+1)}F\left[\frac{\nu}{\nu_m}\frac{\gamma_m^2}{\gamma^2}\right]d\frac{\gamma}{\gamma_m}\\
&= \frac{(p+2)}{8\pi\nu^2}\frac{e^3B}{m_e^2c^2}N_m\int\left(\frac{\gamma_m^2}{\gamma^2}\right)^{\frac{(p+1)}{2}}F\left[\frac{\nu}{\nu_m}\frac{\gamma_m^2}{\gamma^2}\right]\frac{-\gamma^3}{2\gamma_m^3}d\frac{\gamma_m^2}{\gamma^2}\\
&= -\frac{(p+2)}{16\pi\nu^2}\frac{e^3B}{m_e^2c^2}N_m\int\left(\frac{\gamma_m^2}{\gamma^2}\right)^{\frac{(p-2)}{2}}F\left[\frac{\nu}{\nu_m}\frac{\gamma_m^2}{\gamma^2}\right]d\frac{\gamma_m^2}{\gamma^2}\\
&= -\frac{(p+2)}{16\pi\nu^2}\frac{e^3B}{m_e^2c^2}N_m\left(\frac{\nu}{\nu_m}\right)^{-p/2}\int\left(\frac{\nu}{\nu_m}\frac{\gamma_m^2}{\gamma^2}\right)^{\frac{(p-2)}{2}}F\left[\frac{\nu}{\nu_m}\frac{\gamma_m^2}{\gamma^2}\right]d\left(\frac{\nu}{\nu_m}\frac{\gamma_m^2}{\gamma^2}\right)\\
&= \frac{(p+2)}{16\pi\nu^2}\frac{e^3B}{m_e^2c^2}N_m\left(\frac{\nu}{\nu_m}\right)^{-p/2}F_2\left[\frac{\nu}{\nu_m}\right] = \frac{(p+2)(p-1)}{16\pi}\frac{e^3B}{m_e^2c^2}\frac{n}{\gamma_m}\nu_m^{p/2}\nu^{-(p+4)/2}F_2\left[\frac{\nu}{\nu_m}\right]\\
&= \frac{(p+2)(p-1)}{16\pi}n\gamma_m^{p-1}\left(\frac{e^3B}{m_e^2c^2}\right)\left(\frac{eB}{2\pi m_ec}\right)^{p/2}\nu^{-(p+4)/2}F_2\left[\frac{\nu}{\nu_m}\right]
\end{aligned}
\tag{1.26}
$$

Now recalling that for $x \ll 1$ one has $F[x] \propto x^{1/3}$ and that

$$
\int_0^\infty F[y]y^\mu dy = C[\mu] =
\tag{1.27}
$$

one can set

$$
\int_0^x F[y]y^\mu dy = \begin{cases} x^{(3\mu+4)/3}C[\mu] & \text{for}\quad x\le 1\\ C[\mu] & \text{for}\quad x\ge 1\end{cases}
\tag{1.28}
$$

Then:

$$
j_\nu \propto \left(\frac{\nu}{\nu_m}\right)^{\frac{(1-p)}{2}}F_3\left[\frac{\nu}{\nu_m}\right] = \left(\frac{\nu}{\nu_m}\right)^{\frac{(1-p)}{2}}\int_0^{\frac{\nu}{\nu_m}}F[y]y^{(p-3)/2}dy = \begin{cases} \left(\frac{\nu}{\nu_m}\right)^{\frac{1}{3}}C\left[\frac{(p-3)}{2}\right] & \text{for}\quad \nu\le\nu_m\\ \left(\frac{\nu}{\nu_m}\right)^{\frac{(1-p)}{2}}C\left[\frac{(p-3)}{2}\right] & \text{for}\quad \nu\ge\nu_m\end{cases}
\tag{1.29}
$$

$$
\alpha_\nu \propto \left(\frac{\nu}{\nu_m}\right)^{-\frac{(p+4)}{2}}F_2\left[\frac{\nu}{\nu_m}\right] = \left(\frac{\nu}{\nu_m}\right)^{-\frac{(p+4)}{2}}\int_0^{\frac{\nu}{\nu_m}}F[y]y^{(p-2)/2}dy = \begin{cases} \left(\frac{\nu}{\nu_m}\right)^{-\frac{5}{3}}C\left[\frac{(p-2)}{2}\right] & \text{for}\quad \nu\le\nu_m\\ \left(\frac{\nu}{\nu_m}\right)^{-\frac{(p+4)}{2}}C\left[\frac{(p-2)}{2}\right] & \text{for}\quad \nu\ge\nu_m\end{cases}
\tag{1.30}
$$

1.4.2 Synchrotron Spectrum of a Thin Shell

At this point let us assume that the emission comes from a thin shell of radius R and thickness $\delta \ll R$, and that the emissivity and absorption coefficient are constant in the shell. For a line of sight intercepting the shell at a distance r from the center the total intensity will be:

$$
\int_0^{2\delta/\sin\theta} j_\nu e^{-\alpha_\nu x}dx = j_\nu\frac{(1-e^{-\tau_\nu})}{\alpha_\nu}\quad\text{with}\quad\tau_\nu = \frac{2\delta\alpha_\nu}{\sin\theta} = \frac{2\delta\alpha_\nu R}{\sqrt{R^2-r^2}}
\tag{1.31}
$$

Now the average optical depth will be:

$$
\tilde{\tau}_\nu = \frac{2}{R^2}\int_0^R\frac{2\delta\alpha_\nu R}{\sqrt{R^2-r^2}}rdr = 4\delta\alpha_\nu
\tag{1.32}
$$

Hence:

$$
\tilde{\tau}_\nu = \frac{(p+2)(p-1)}{4\pi} \frac{n\delta}{\gamma_m^5} \left(\frac{e^3 B}{m_e^2 c^2} \right) \left(\frac{eB}{2\pi m_e c} \right)^{-2} \times \begin{cases} \left(\frac{\nu}{\nu_m} \right)^{-\frac{5}{3}} C \left[\frac{(p-2)}{2} \right] & \text{for} \quad \nu \le \nu_m \\ \left(\frac{\nu}{\nu_m} \right)^{-\frac{(p+4)}{2}} C \left[\frac{(p-2)}{2} \right] & \text{for} \quad \nu \ge \nu_m \end{cases} \tag{1.33}
$$

The frequency ν_a where $\tilde{\tau}_\nu = 1$ is the synchrotron self-absorption frequency. The total intensity will be:

$$
J_\nu = 4\pi R^2 \delta \frac{(1-e^{-\tilde{\tau}_\nu})}{\tilde{\tau}_\nu} j_\nu = 2\pi R^2 \delta \frac{(1-e^{-\tilde{\tau}_\nu})}{\tilde{\tau}_\nu} \frac{(p-1)n}{\gamma_m^{1-p}} \left(\frac{e^3 B}{m_e^2 c^2} \right) \times \begin{cases} \left(\frac{\nu}{\nu_m} \right)^{\frac{1}{3}} C \left[\frac{(p-3)}{2} \right] & \text{for} \quad \nu \le \nu_m \\ \left(\frac{\nu}{\nu_m} \right)^{\frac{(1-p)}{2}} C \left[\frac{(p-3)}{2} \right] & \text{for} \quad \nu \ge \nu_m \end{cases} \tag{1.34}
$$

Now if $\nu_a < \nu_m$ then:

$$
J_\nu \propto \begin{cases} \nu^2 & \text{for} \quad \nu < \nu_a \\ \nu^{1/3} & \text{for} \quad \nu_a < \nu < \nu_m \\ \nu^{(1-p)/2} & \text{for} \quad \nu > \nu_m \end{cases} \tag{1.35}
$$

If instead $\nu_a > \nu_m$ then:

$$
J_\nu \propto \begin{cases} \nu^2 & \text{for} \quad \nu < \nu_m \\ \nu^{5/2} & \text{for} \quad \nu_m < \nu < \nu_a \\ \nu^{(1-p)/2} & \text{for} \quad \nu > \nu_a \end{cases} \tag{1.36}
$$

1.4.3   Sedov evolution

Once the expansion speed drops below the speed of light the evolution of the system follows the standard Sedov solution:

$$
R(t) = \left(\frac{E}{\rho} \right)^{1/5} t^{2/5}, \qquad \dot{R}(t) = \frac{2}{5} \frac{R(t)}{t} = \frac{2}{5} \left(\frac{E}{\rho} \right)^{1/5} t^{-3/5} \tag{1.37}
$$

where E is the energy of the explosion, and ρ is the ambient density (a different scaling applies if instad of a uniform ISM one consider a wind with $\rho \propto r^{-2}$). Give the self-similarity of the Sedov solution, we can assume that the magnetic energy density downstream of the shock is a fixed fraction of the thermal pressure. Then:

$$
\frac{B^2}{8\pi} = \epsilon_{\rm B} \rho \dot{R}^2 \mathcal{P}(r/R(t)) \quad \Rightarrow \quad B \propto (t/t_o)^{-3/5} \tag{1.38}
$$

where $\mathcal{P}(r/R(t))$ describes the profile of the thermal pressure with radius and ranges from $3/4$ at the forward shock in $R(t)$ to $1/4$ at the center, and $\epsilon_{\rm B} \le 1$ tells us how magnetized the system is. Analogously we can assume that the energy density of the non-thermal emitting electrons is a constant fraction of the total thermal energy. Assuming a power-law distribution with a minimum energy $\gamma_{\rm min} m_e c^2$, and power la index $p > 2$ one has:

$$
\int_{\gamma_{\rm min}}^\infty N_m (\gamma/\gamma_{min})^{-p} \gamma m_e c^2 d\gamma = \epsilon_{\rm e} \rho \dot{R}^2 \mathcal{P}(r/R(t)) \quad \Rightarrow \quad \frac{N_m m_e c^2}{p-2} \gamma_{\rm min}^2 = \epsilon_{\rm e} \rho \dot{R}^2 \mathcal{P}(r/R(t)). \tag{1.39}
$$

$$
\Rightarrow \quad \frac{p-1}{p-2} \gamma_{\rm min} n = \epsilon_{\rm e} \frac{\rho \dot{R}^2}{m_e c^2} \mathcal{P}(r/R(t)). \tag{1.40}
$$

where, we made use of Eq. 1.20, and $\epsilon_{\rm e} \le 1$ tells us what fraction of the plasma energy is carried by the non-thermal emitting particles. It is reasonable to assume that the characteristic energy of the radiating particles scales

as the characteristic energy of the incoming matter, and that their density scales as the incoming ambient density $n \propto \rho$, then:

$$\gamma_{\min} \propto \dot{R}^2 \quad \Rightarrow \quad \gamma_{\min} \propto (t/t_o)^{-6/5}, \quad \Rightarrow \quad \nu_{\min} \propto (t/t_o)^{-3} \tag{1.41}$$

Hence, if coherently with the Sedov self similar scaling we take $\delta \propto R \propto t^{2/5}$ the spectrum will have the following scalings: if $\nu_a < \nu_m$ then:

$$J_\nu \propto \begin{cases} \nu^2 t^{-2/5} & \text{for} \quad \nu < \nu_a \\ \nu^{1/3} t^{8/5} & \text{for} \quad \nu_a < \nu < \nu_m \\ \nu^{(1-p)/2} t^{3(7-5p)/10} & \text{for} \quad \nu > \nu_m \end{cases} \tag{1.42}$$

if instead $\nu_a > \nu_m$ then:

$$J_\nu \propto \begin{cases} \nu^2 t^{-2/5} & \text{for} \quad \nu < \nu_m \\ \nu^{5/2} t^{11/10} & \text{for} \quad \nu_m < \nu < \nu_a \\ \nu^{(1-p)/2} t^{3(7-5p)/10} & \text{for} \quad \nu > \nu_a \end{cases} \tag{1.43}$$

This shows that the temporal evolution of the spectrum allows one to identify the Sedov phase.

1.4.4 Calorimetry

From Eq. 1.34 one sees that at any one time the spectrum if fully determined by the following parameters: n (or alternatively ϵ_e), γ_m, p, B (or alternatively ϵ_B), R, δ. The spectral slopes (directly related to p) and breaks (if identified with the ν_m and ν_a), together with the spectral normalization allow one to fix four of these parameters as a function of the remaining two. In general since n and δ always enter together as $n\delta$ they can be factored into a single parameter (δ itself can be set equal to ηR with $\eta \leq 1$). It is thus possible to express these various quantities, for example the magnetic field, just as a function of the unknown radius. However by measuring the spectrum at two different times t_1 and t_2, it is known that the radii must scale as: $R_2/R_1 = (t_2/t_1)^{2/5}$. If the radii are correct then one should recover also the correct scalings for other derived quanties like B or γ_m. Once the radius is known, then E/ρ is also known. If one can derive ρ from other observables, of one has some idea of the possible values of the density in the ambient medium of a GRB, it is then possible to constrain E.
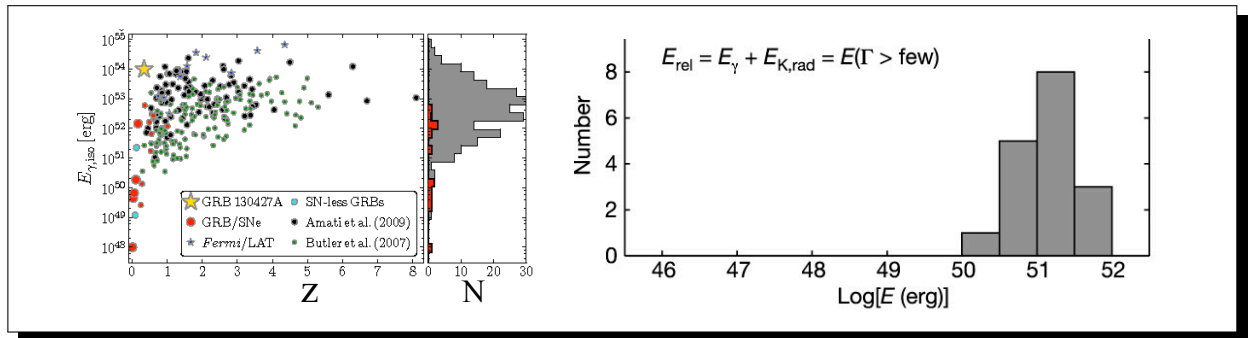
Figure 1.17: Left panel: distribution of the isotropic γ-ray energy of the prompt emission. Right panel: distribution of the total energy of the explosion inferred from late time calorimetry and beaming corrected for jet-break, for a set of GRBs.

It is found, see Fig. 1.17 that the typical total energy involved in GRBs is of the order of 10^{51} erg, comparable to the typical energy of a SN, with typical upper limit $\sim$ a few 10^{52}erg. This suggest that the jet solid angle is $\sim 4\pi/100$, corresponding to an opening angle $\lesssim 10°$.

CHAPTER 2

THE FIREBALL MODEL

2.1 The Fireball Idea

As we discussed the observed millisecond time variability of GRBs, immediately points toward a compact engine, of typical size $r_i \simeq 10^7$ cm. On the other hand the duration of the prompt emission $\sim 1 - 100$ s, suggests that energy injection is not impulsive but is continuous on the timescale of the engine. the large amount of energy confined within such a small volume can be described as a *fire-ball*. The term fireball refers to any system where the energy density is so high that photond are in thermal equilibrium with a plasma of electrons and positrons, at typical relativistic conditions.

2.1.1 Conditions at injection

The typical temperature at the base of the central engine at what is known as the injection radius can be computed recalling that GRBs are associated to the gravitational collapse of the core of a massive progenitor or the merging of a binary NS. In both cases we are dealing with a mass of the order of $1.5 - 3M_\odot$. The energy involved in both events are of the order of the gravitational binding energy $GM^2/R \simeq 5 \times 10^{53}$ erg, where typical radii are $\sim 10^6$ cm. Not all of this energy ends in the GRB. Most of it is radiated away, in the form of GWs, and neutrinos, which are decoupled form matter. Only a fraction $\sim 10^{-2}$ thermalizes into a fireball of $e^\pm$ pairs and high energy photons, with a typical black body temperature at the injection radius r_i:

$$
\frac{4\pi r_i^3}{3} \frac{4\sigma_{\rm sb}}{c} T_i^4 \simeq 10^{-2} \frac{GM^2}{R} \quad \Rightarrow T_i \simeq \begin{cases} 10^{11} \left(\frac{M}{1.5M_\odot}\right)^{1/2} \left(\frac{10^6 {\rm cm}}{R}\right)^{1/4} \left(\frac{10^7 {\rm cm}}{r_i}\right)^{3/4} {\rm K} \\ 10 \left(\frac{M}{1.5M_\odot}\right)^{1/2} \left(\frac{10^6 {\rm cm}}{R}\right)^{1/4} \left(\frac{10^7 {\rm cm}}{r_i}\right)^{3/4} {\rm MeV} \end{cases} \quad (2.1)
$$

The black-body thermal energy is much higher than the rest mass energy of $e^\pm$, such that there will be copious pair production. The system is also optically thick for photon propagation. The typical baryon density at the base of the engine can be computed recalling that ultimately baryons (protons) are accelerated up to Lorentz factor $\gamma_{\rm GRB} \sim 500 - 1000$. This implies that the average energy per baryon should be:

$$
10^{-2} \frac{GM^2}{R} \simeq \gamma_{\rm GRB} n_p m_p c^2 \frac{4\pi r_i^3}{3} \quad \Rightarrow \quad n_p \simeq 2 \times 10^{30} \left(\frac{M}{1.5M_\odot}\right)^2 \left(\frac{10^6 {\rm cm}}{R}\right) \left(\frac{10^7 {\rm cm}}{r_i}\right)^3 {\rm cm}^{-3} \quad (2.2)
$$

2.1.2 Pair creation

We are going to begin our characterization of the fireball with a discussion of the equilibrium properties of the reaction $e^+e^- \leftrightarrow \gamma\gamma$. We recall that the chemical potential μ is defined as the energy change with particle number at fixed volume and entropy:

$$dU = TdS + \mu dN \tag{2.3}$$

and μ represents the amount of energy required to increase by one the numer of particles in a closed system. We see immediately that $\mu = (dU/dN)_{T=0}$, the energy required to add a particle at zero temperature. Photons have zero chemical potential (it takes zero energy to add a photon to a black-body at zero temperature). On the other hand fermions have a non-zero chemical potential due to Pauli's exclusion principle, and to the fact that they have a finite rest mass. The equilibrium condition will then reads $\mu_+ + \mu_- = 0$. Now for electron and positrons following Fermi-Dirac statistic, the chemical potential can be related to the density and temperature by:

$$n = 2 \int_o^\infty \frac{4\pi p^2 dp}{(2\pi\hbar)^3} \frac{1}{e^{(\epsilon-\mu)/kT} - 1} \quad \rightarrow \quad \int_o^\infty \frac{8\pi p^2}{(2\pi\hbar)^3} \frac{e^{\mu/kT}}{e^{\epsilon/kT}} dp \quad \text{in the classical limit} \tag{2.4}$$

where the energy $\epsilon = c\sqrt{p^2 + m^2 c^2}$. In the relativistic ($\epsilon = cp$) and non relativistic ($\epsilon = mc^2 + p^2/2m$) regime one has:

$$n = 2 \left(\frac{kT}{c\hbar}\right)^3 \frac{1}{\pi^2} e^{\mu/kT} \qquad \text{and} \qquad n = 2 \left(\frac{mkT}{2\pi\hbar^2}\right)^{3/2} e^{(\mu-mc^2)/kT} \tag{2.5}$$

now using the equilibrium condition on the chemical potentials one finds:

$$n_+ n_- = 4 \left(\frac{kT}{c\hbar}\right)^6 \frac{1}{\pi^4} \qquad \text{and} \qquad n_+ n_- = 4 \left(\frac{mkT}{2\pi\hbar^2}\right)^3 e^{-2mc^2/kT} \tag{2.6}$$

Now if n_o is the number of electrons in the absence of pair production (the electron excess) then one has $n_- - n_+ = n_o \Rightarrow n_+^2 + n_o n_+ - n_+ n_- = 0$. This is just a second-order equation that can be solved for $n+ =$ to give:

$$2n_+ + n_o = \left[n_o^2 + 2 \left(\frac{mc}{\hbar}\right)^6 \left(\frac{kT}{\pi mc^2}\right)^3 e^{-2mc^2/kT}\right]^{1/2} \qquad \text{for} \quad kT < mc^2 \tag{2.7}$$

$$2n_+ + n_o = \left[n_o^2 + \frac{16}{\pi^4} \left(\frac{mc}{\hbar}\right)^6 \left(\frac{kT}{mc^2}\right)^6\right]^{1/2} \qquad \text{for} \quad kT > mc^2 \tag{2.8}$$

$$\tag{2.9}$$

The temperature at which $n_+ = n_o$ (or equivalently the density of the unpaired electrons n_o below which the density of pairs due to photon pair production/annihilation is larger) can be considered as the reference temperature (density) for efficient pair-radiation coupling. One has in the relativistic and non-relativistic regime:

$$2\sqrt{2}n_o = \frac{4}{\pi^2}\lambda_c^{-3} \left(\frac{kT}{mc^2}\right)^3 \quad \Rightarrow \quad n_o = 2.6 \times 10^{30} \left(\frac{kT}{mc^2}\right)^3 \text{cm}^{-3} \tag{2.10}$$

$$2\sqrt{2}n_o = \sqrt{\frac{2}{\pi^3}}\lambda_c^{-3} \left(\frac{kT}{mc^2}\right)^{3/2} e^{-mc^2/kT} \quad \Rightarrow \quad n_o = 1.6 \times 10^{30} \left(\frac{kT}{mc^2}\right)^{3/2} e^{-mc^2/kT}\text{cm}^{-3} \tag{2.11}$$

which can be used to establish if there is or not efficient pair-production coupling. It is evident that for $T > mc^2$ pair-production will be efficient even at densities $\rho = m_p n_o > 4 \times 10^6$ g cm^{-3}. If instead one considers the non relativistic limit one finds that the threshold ranges from $kT/mc^2 \simeq 0.011$ for $n_o \simeq 10^{-10}$ cm^{-3}, to $kT/mc^2 \simeq 0.016$ for $n_o \simeq 1$ cm^{-3}, and $kT/mc^2 \simeq 0.05$ for $n_o \simeq 10^{20}$ cm^{-3}.

For $kT \simeq 10\text{MeV}$ the threshold density is $n_o = n_p \simeq 2 \times 10^{34}$ cm $^{-3}$ much higher than the typical proton density at the base of the engine given by the estimate Eq. 2.2, which instead give a typical coupling temperature $kT \simeq 1\text{MeV}$.

One can compute the typical number density of pairs in the limit $kT \gg m_e c^2$ and the reasult is:

$$n_{\pm} \approx \frac{2}{\pi^2} \left(\frac{kT}{\hbar c} \right)^3 \qquad (2.12)$$

this is comparable with the typical photon density:

$$n_{\gamma} \approx \frac{\pi^2}{15} \left(\frac{k^4 T^4}{\hbar^3 c^3} \right) \frac{1}{h\nu_{\max}} \approx \frac{\pi^2}{45} \left(\frac{kT}{\hbar c} \right)^3 \qquad (2.13)$$

and for temperatures of the order of 10 Mev the typical densities are $\sim 10^{34}$ cm $^{-3}$, $\gg n_p$.

2.1.3 Optical Depth

One can then check the optical thickness of the injection region for processes involving pair and photon scattering. The three main processes that define the mean free path for pairs and photons, are pair creation/annihilation and Compton scattering. The cross section for these processes are shown in Fig. 2.1, and, as one can see, at the typical energies of interest $E \sim 10\text{MeV}$, they ranges between 10^{-3} to 10^{-2} times the Thompson cross section.
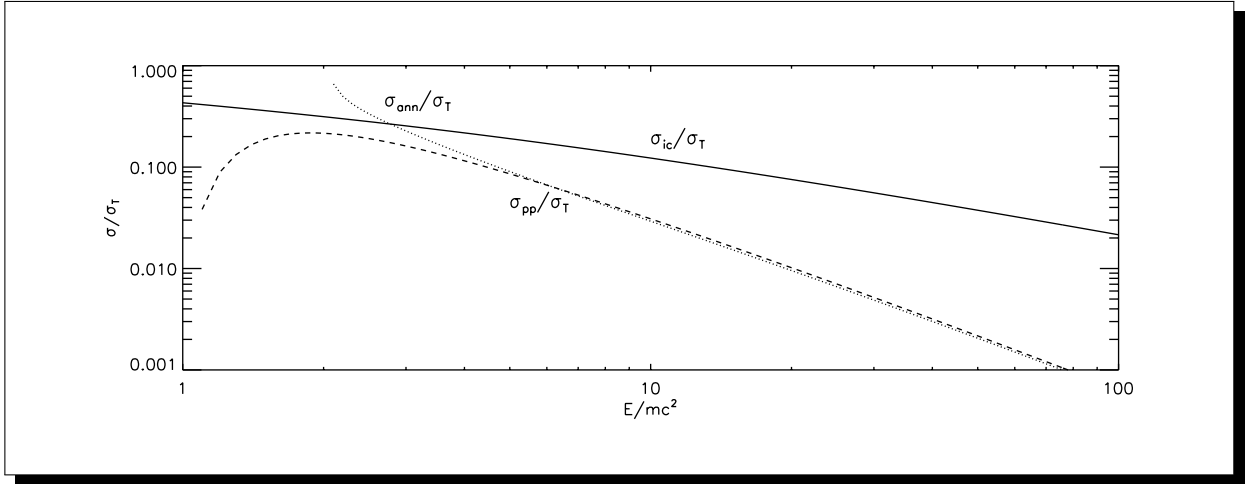

Figure 2.1: Cross sections for pair annihilation (dotted line), photon-photon pair production (dashed line) and inverse compton scattering (solid line), with respect to the Thompson cross section, given as a function of the "center of mass" total energy.

The photon mean free path, for Thompson/Compton scattering, considering that at $T = 10$ MeV $n_{\pm} \approx 10^4 n_o = 10^4 n_p \sim 10^{34}$ cm^{-3}, will be:

$$1/n_{\pm}\sigma_{\text{ic}} \approx 7 \times 10^{-10}\text{cm} \ll r_i \qquad (2.14)$$

such that the depth is $\tau \sim 10^{16}$. The pair mean free path for electron positron annihilation will be:

$$1/n_{\pm}\sigma_{\text{ann}} \approx 7 \times 10^{-9}\text{cm} \ll r_i \qquad (2.15)$$

and again the depth is $\tau \sim 10^{15}$.

The photon mean free path for photon-photon pair production is instead:

$$1/n_\gamma \sigma_{\mathrm{pp}} \approx \frac{E}{V} \frac{1}{h\nu_{\max}} \frac{1}{\sigma_{\mathrm{pp}}} \approx 10^{-2} \frac{GM^2}{R} \frac{3}{4\pi r_i^3} \frac{1}{2.82 k_{\mathrm{b}} T} \frac{1}{\sigma_{\mathrm{pp}}} \approx 4 \times 10^{-9} \mathrm{cm} \ll r_i \tag{2.16}$$

where we have taken $h\nu_{\max} \sim 10\mathrm{MeV} \to T \sim 10^{11}\mathrm{K}$. This again implies an optical depth for pair creation $\tau \sim 10^{15}$. The mean free paths at the source justify the assumption of thermal equilibrium and high scattering/interaction depth for pairs and photons.

With this conditions the plasma at the central engine can be described as a *fireball*.

2.2 Dynamical evolution of a fireball

Given the temperature and energy of the fireball at injection one immediately see that the system will rapidly expand at relativistic speed. At the very base of the system $r \sim r_i$ the typical outflow speeds will be of the order of the twermal speed of the fireball $T \sim 10\mathrm{MeV} \Rightarrow \gamma \sim 10$. The observed variability suggests that in many cases we are not dealign with a smooth continuous flow, but with the ejection of clump (shells) of matter. In principle each of these shell will have sligthly different conditions, and will undergo different acceleration as it expands, with respect to the preceeding and following one. One can the consisder the typical average condition of the shells and then check how their differences impact on the evolution.

2.2.1 Expansion

As we have seen, in order to accelerate a relativistic outflow, the ratio of the energy of the gas E over its mass M should be much larger than unity.

We assume that the fireball produced by the central engine central engine, can be described in terms of a series of shells (or blobs) that are emitted at an injection radius r_i, with Lorentz factor $1 \ll \gamma_i \ll E/Mc^2$. Let Δ be the typical thickness of these shells. Then one can write mass, entropy and energy conservation for a single shell as:

$$r^2 \gamma \rho \Delta = r_i^2 \gamma_i \rho_i \Delta_i \tag{2.17}$$

$$r^2 \gamma e^{3/4} \Delta = r_i^2 \gamma_i e_i^{3/4} \Delta_i \tag{2.18}$$

$$r^2 \gamma^2 (\rho + 4e/3) \Delta = r_i^2 \gamma_i^2 (\rho_i + 4e_i/3) \Delta_i \tag{2.19}$$

where e is the net internal energy and we have assumed a relativistic gas with $p = e/3$, and $\gamma \gg 1$.

2.2.1.1 Radiation Dominated Phase We make at this point the so called *frozen spike approximation* $\Delta = \Delta_i$. Initially one starts with a relativistically hot plasma with $e_i/\rho_i \simeq E/Mc^2 \gg 1$ (where we assume that the typical energy per baryon of the various shells is of the same order) . Then one can write:

$$r^2\gamma\rho = const, \qquad r^2\gamma e^{3/4} = const, \qquad r^2\gamma^2 e = const. \tag{2.20}$$

giving:

$$e = e_i(r/r_o)^{-4}, \qquad \rho = \rho_i(r/r_i)^{-3}, \qquad \gamma = \gamma_i(r/r_i) \tag{2.21}$$

This is the radiation dominated phase, during which the Lorentz factor increases proportionally to the radius, and that last until $e/\rho \simeq 1 \Rightarrow r = r_i(e_i\rho_i)$. Which defines the so called saturation radius and Lorenz factor:

$$R_\mathrm{s} = r_i(E/Mc^2) \simeq 5 \times 10^9 \, R_{i7}E_{52}/M_{-5} \, \mathrm{cm} \qquad \gamma_\mathrm{s} = \gamma_i(E/Mc^2) \simeq 500\gamma_i E_{52}/M_{-5} \tag{2.22}$$

where we have se $E_{52} = E/10^{52}$ erg s^{-1}, and $M_{-5} = M/10^{-5}M_\odot$.

2.2.1.2 Matter Dominated Phase At $r = R_\mathrm{s}$ the outflow enters the matter dominated phase. In the frozen-spike approximation one can write:

$$r^2\gamma\rho = const, \qquad r^2\gamma e^{3/4} = const, \qquad r^2\gamma^2\rho = const. \tag{2.23}$$

giving:

$$e = e_\mathrm{s}(r/R_\mathrm{s})^{-3/8}, \qquad \rho = \rho_\mathrm{s}(r/R_\mathrm{s})^{-2}, \qquad \gamma = \gamma_\mathrm{s} \tag{2.24}$$

where e_s, ρ_s and γ_s are evaluated at the saturation radius. In the matter dominated phase the frozen-spike approximation does not holds at all radii. Once it breaks $\Delta \propto r$ and one has:

$$e = e_\mathrm{s}(r/R_\mathrm{s})^{-4}, \qquad \rho = \rho_\mathrm{s}(r/R_\mathrm{s})^{-3}, \qquad \gamma = \gamma_\mathrm{s} \tag{2.25}$$

showing that the Lorentz factor remain constant at the saturation value.

2.2.2 Internal Dissipation

First we are going to show that during the radiation dominated phase, the frozen spike approximation holds. Let us assume that a shell is injected with typical average Lorentz factor γ_i, and a typical thickness $\Delta_i = c\delta t_i \simeq r_i = ct_i$ from each other. Now in general the front and back sides of the shell (f and b) will be injected with different Lorentz factor $\gamma_{fi} \simeq \gamma_{bi} \simeq \gamma_i \gg 1$. Assume that back side b is injected with a lower Lorentz factor than the front f, and that each evolve according to Eq. 2.25 so that in principle the thickness will increase (but the math can be repeated in the other case leading to the same result). Then:

$$\delta\gamma = \gamma_f - \gamma_b = \gamma_{fi}\frac{r_f}{r_i} - \gamma_{bi}\frac{r_b}{r_i} = \gamma_{fi}\frac{r}{r_i} - \gamma_{bi}\frac{r}{r_i} + \frac{\gamma_{fi} + \gamma_{bi}}{2}\frac{\Delta}{r_i} \tag{2.26}$$

$$\simeq \delta\gamma_i\frac{r}{r_i} + \gamma_i\frac{\Delta}{r_i} = \gamma_i\left[\eta_\gamma\frac{r}{r_i} + \frac{\Delta}{r_i}\right] \simeq \gamma_i\eta_\gamma\frac{r}{r_i} = \eta_\gamma\gamma \tag{2.27}$$

where we have set $r_b = r - \Delta/2, r_f = r + \Delta/2$, $\eta_\gamma = (\gamma_{2i} - \gamma_{1i})/\gamma_i \lesssim 1$, and we have set $\Delta \ll r$. This difference in Lorentz factor corresponds to a different velocity δv. Now for a relativistic flow:

$$v = \sqrt{1 - \gamma^{-2}} \simeq 1 - 1/2\gamma^2 \quad \Rightarrow \quad \delta v = \frac{\partial v}{\partial\gamma}\delta\gamma = \frac{\delta\gamma}{\gamma^3} \simeq \frac{\eta_\gamma}{\gamma^2} \tag{2.28}$$

Then the shell thickness will evolve according to $d\Delta/dt = \delta v$, as:

$$\Delta(t) = \Delta_i + \int_o^t \delta v\, dt = \int_o^t \frac{\eta_\gamma}{\gamma^2} dt = \Delta_i + \int_{\gamma_i}^\gamma \frac{\eta_\gamma}{\gamma^2} \frac{t_i}{\gamma_i} d\gamma = \Delta_i + \eta_\gamma \frac{t_i}{\gamma_i} \left[\frac{1}{\gamma_i} - \frac{1}{\gamma} \right] < \Delta_i + \eta_\gamma \frac{t_i}{\gamma_i^2} \qquad (2.29)$$

$$\Delta(t) < \Delta_i + \eta_\gamma \frac{r_i}{\gamma_i^2} \simeq \Delta_i[1 + \eta_\gamma/\gamma_i^2] \simeq \Delta_i \qquad (2.30)$$

In the same way we can show that during the radiation dominated phase, the various shells do not interact among them, so that each evolve as an isolated one. We just need to repeat the previous math substituting the shell thickness Δ with the shell separation Λ, and consider the case of two shells emitted in succession with $\delta t_i = \Lambda/c$, and with the inner one going at a higher Lorentz factor, so that in principle it can catch up with the previous. The final result will be the same

$$\Lambda(t) =< \Lambda_i + \eta_\gamma \frac{r_i}{\gamma_i^2} \simeq \Lambda_i[1 + \eta_\gamma/\gamma_i^2] \simeq \Lambda_i \qquad (2.31)$$

So we can conclude that during the radiation dominated phase each shell evolve as an isolated structure of constant thickness such that neither inner (in the shell) nor intra (among shells) dissipation take place.

For the matter dominated phase instead one has:

$$\delta\gamma = \eta_\gamma \gamma_s \quad \Rightarrow \quad \delta v = \eta_\gamma \frac{1}{\gamma_s^2} \quad \Rightarrow \quad \Delta(t) = \Delta_i + \eta_\gamma \frac{ct - ct_s}{\gamma_s^2} = \Delta_i + \eta_\gamma \frac{r - R_f}{\gamma_s^2} \qquad (2.32)$$

this set the limit for the application of the frozen -spike approximation:

$$R_d = R_s + \frac{\Delta_i}{\eta_\gamma} \gamma_s^2 \qquad (2.33)$$

for $\eta_\gamma \sim 1$, and $\Delta_i \sim r_i \sim 10^7$cm, we have $R_d \sim 10^{11}$ cm. This is about a factor 10 laerger than the typical radii of carbon-oxygen WR star whose core has just collapsed. At such distance the variious shells will begin to interact. This interaction will dissipate the relative internal energy and lead to emission. This mechanism is known as *internal shocks model*, and it is invoked to expalin the prompt γ-ray emission.

2.2.3 Slow-down

The coasting phase, where the system expands at a constant Lorentz factor (apart from the interaction of the various shells that only dissipate the relative energy) will last as long as the swept-up mass is mall enough not to affect the dynamics.

The flow will begin to slow down once the condition:

$$\frac{4\pi}{3} n m_p (ct_{sl})^3 \gamma_{mrs}^2 c^2 = E \qquad (2.34)$$

is met. Puttign typical values for the energy, and the ISM density one finds radii od the order of 10^{16} cm, corresponding to a typical time ~ 1 day. This set the beginning of the so called X-ray afterglow, which is mostly due to the emission of the shock front propagating in the surrounding medium, and that can be described using the Blandford-McKee solution:

$$\gamma(t) = \left(\frac{3E}{256\pi n m_p c^2} \right)^{1/8} t^{-3/8} \qquad (2.35)$$

2.2.4 Newtonian Timescale

When the Lorentz factor reaches unity the system enters the Newtonian phase, when iy will evolve according to the standard Sedov solution. The Newtonian timescale is set by:

$$t_{\text{Newt}} = \left(\frac{3E}{256\pi n m_p c^2} \right)^{1/3} \tag{2.36}$$

corresponding to typical timescales of a few hundreds days.